Effect of gas pulses on transport in NBI plasmas of the TJ-II stellarator

M. A. Ochando[1], D. López-Bruna[1], J. J. Martinell[2], F. L. Tabarés[1] and D. Tafalla[1].

1-Laboratorio Nacional de Fusión, Ciemat, 28040 Madrid, Spain
2-Instituto de Ciencias Nucleares, UNAM, Mexico D.F., Mexico

E-mail: ma.ochando@ciemat.es

Abstract. The experimental evolution of low-density (~10^{19} m^{-3}) NBI plasmas of the TJ-II Heliac-type stellarator in response to short gas-puff pulses is simulated with a transport model that includes elements for transport barrier formation, neoclassical radial electric field and the evolution of three carbon charge-states. Two typical phenomena following a gas pulse are described: the formation of pivot points in the emissivity profiles as a consequence of transport barrier formation processes, and the smooth confinement change due to changes in the neoclassical transport caused by the forced modification of plasma profiles.

1. Introduction

As it is well known, plasma composition is one critical issue that must be controlled to drive plasmas to good confinement conditions. The nature of incoming impurities and their amount are restricted and limited, depending on the temperature attainable in each device. Avoiding high- to medium-Z impurities has been the general trend to eliminate such efficient energy sinks that can impede the access to the H-mode confinement regime or lead plasmas of medium-size machines to collapse.

In the TJ-II stellarator, full lithium wall-coating has enabled density control and distinguishing the passage to improved confinement regimes, say H-mode, from a well established L-mode base plasma. In previous works [1, 2], we have reported on experiments to control the shape of the electron density profile in neutral beam injection (NBI) heated plasmas using different base-gas puffing schemes and/or injecting short pulses of low-Z impurity species. Series of reproducible discharges were produced to study the progressive change in confinement conditions as gas pulse lengths were increased. A common observation in low-NBI input power discharges is that right after the gas injection, the volume averaged electron temperature decreased, the central soft x-ray emissions notably fell and radiation from plasma periphery sharply increased. This response was qualitatively interpreted in terms of enhanced peripheral charge-exchange processes with impurities (mainly carbon) that may diminish the coupling of fast neutrals with the plasma core. Now, a transport model based on balance equations for the densities of electrons and electron and ion kinetic energies is used to check the interpretation from a quantitative perspective. The transport simulations are only intended to reproduce acceptably the experimental plasmas with as much physics-based modelling as presently possible, but two ingredients are fundamental in order to discuss the experiments: the self-consistent neoclassical radial electric field and a mechanism for transport barrier formation/destruction. Even though the details of atomic physics are still not addressed, it is found that the changes in transport properties are an important piece to explain the effect of gas pulses on plasma evolution.

The remainder of the paper is organized as follows. Section 2 describes the plasma response to the puffing of a gas pulse: the transient passage of the density and radiation emissivity profiles through dome-type shape [3], often found when a transport barrier develops (2.1). The numerical results are presented in Section 3 starting with a description of the transport model with which the phenomena are described (3.1); then the reference and the close to critical cases of sub-section 2.1 are simulated respectively in 3.2 and 3.3; and the smooth establishment, during several confinement times at least, of a different confinement regime without detected transport barriers is presented in 3.4. The discussion and brief conclusions are exposed in Section 4.

2. Experimental data

The experiments have been performed in the TJ-II stellarator [4], a 4-period Heliac-type device with 1.5 m and ~ 0.2 m of major and minor radii, using a magnetic configuration with confining volume of about 1 m^3 and vacuum rotational transform $1.55 \leq \iota(\rho) \leq 1.65$, being ρ the normalized radial coordinate (proportional to the square root of the enclosed plasma volume). The discharges here described start with low-density (< 10^{19} m^{-3}) electron-cyclotron resonance heating (ECRH) plasmas that are used as target for NBI. Since the density is an effective knob for the establishment of near-edge transport barriers causing edge cooling that easily drive the plasma to radiative collapse [5], the target plasmas for the gas-pulse experiments have been operated with lithium-coated wall to allow for the creation of peaked, low to moderate density plasmas (line average $\leq 2 \cdot 10^{19}$ m^{-3}) close to steady state. Such density profiles are typical of the TJ-II L-mode of confinement under NBI heating. In these conditions, the gas flow during the pulses is controlled through the voltage pre-programmed in the gas valves. If the pulses are too weak, the perturbation of the density fades away in a time comparable with the expected confinement time. For strong pulses, the plasmas can undergo a transition to H-mode that normally ends rapidly after excessive radiative cooling. For intermediate pulses, as those described below, two kinds of significant response have been found: either the plasma is forced to transiently abandon the peaked (bell) shape to become wider (dome), or the plasma smoothly changes transport properties without showing traces of bifurcation in confinement mode.

As our Thomson scattering (TS) system is single-pulse [6], to monitor the detailed time evolution of plasma profiles we usually produce a high number of repetitive discharges and fire the laser pulse at different time instants. However, as it was shown in a previous work [7] using a wide database of Thomson scattering profiles from discharges produced in many magnetic configurations, the peaking factor of the total radiation profile follows the electron density profile tendency. Therefore, we have used the total emissivity profiles, reconstructed by tomographic inversion [8] of the line integral radiation signals obtained with the TJ-II bolometry system [9], both to illustrate the behaviour of the radiation itself and to help in the simulations when no TS profiles are available.

2.1 Transient dome-shaped profiles

In series of reproducible discharges, started with ECRH heating (500 kW, 2nd harmonic X-mode) and afterwards heated and fuelled with a co-injected neutral beam (430 kW port-through), H_2 pulses of different lengths were injected to modify plasma profiles (particle fluxes $7 \cdot 10^{20}$ e/s < Q_{in} < $35 \cdot 10^{20}$ e/s). Injections in the path of the beam and far from it were performed to check for different behaviours in radiation signals. Apart from the Hα monitors, no toroidal variations were found. In Figure 1 we have plotted the complete time traces of average electron density, energy content (as measured with one diamagnetic loop), intensity of the 227 nm C_V line and total radiated power from some perturbed and reference discharges belonging to three series of shots heated with co-NBI only. There, it can be seen that for all levels of working electron density (ranging from about 1×10^{19} m^{-3} to 2×10^{19} m^{-3}) and independently of the pulse injection time (or toroidal location), it was possible to obtain discharges that rapidly reach a rather stable level of higher density. The bottom boxes show the magnetic fluctuations power spectra of the three reference discharges. It is apparent that the patterns of coherent fluctuations are almost identical and characteristic of L-mode discharges produced in this magnetic configuration under freshly Li-coated vacuum chamber wall. In detailed studies performed in plasmas of this kind we found that the confinement state is well related to the behaviour of low frequency coherent modes associated with the rotation of near-edge magnetic islands. In brief (see [10, 11]), a coherent low frequency (~20–30 kHz in these cases) mode is associated with L-mode plasmas, a threshold state between L- and H-mode is characterized by unstable chirping-down mode at higher frequencies (~ 60–90 kHz), and the low frequency coherent rotation mode is recovered, although much dimmed if at all detected, during the H-mode (see also in [12] a statistical study of the relationship between confinement transitions and MHD activity in plasmas with similar magnetic configurations).

As we have mentioned above, intermediate intensity injections may provide a tool to modify, in a controlled manner, not only plasma profiles, but the confinement state. We will focus on the series with the highest base density, consisting of nine shots, from which three discharges, namely #24001, the reference case, and #24006 and #24009, the perturbed cases, will be presented here more in detail and simulated with the transport model in next section.

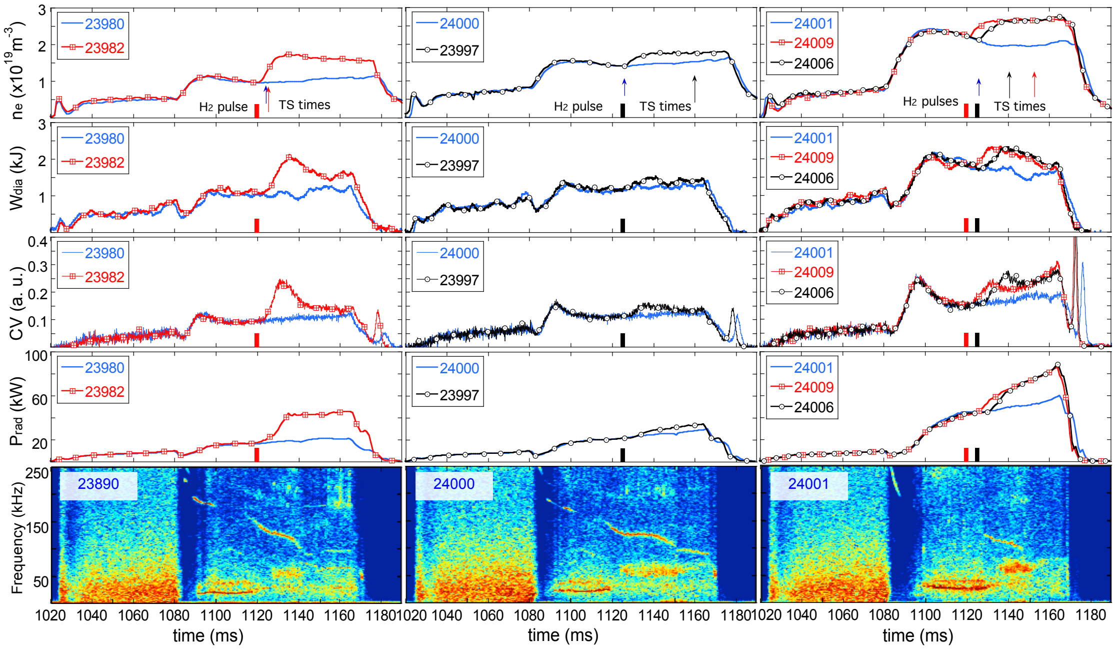

Figure 1. Time evolution of the line averaged density, global energy content (as measured with diamagnetic loops), intensity of the 227 nm C_V line collected far from the pulse injection ports, and total radiated power of seven TJ-II discharges (heated with 500 kW of ECRH until 1080 ms and with 450 kW (co-injected NBI), representative of three studied series. Reference (non-perturbed) discharges of each series, with different initial density in the pre-pulse phase, are represented by the continuous light blue line, perturbed discharges are represented by continuous lines with markers, either red crossed squares or black open circles. Hydrogen is puffed in the perturbed shots through two different ports and the entrance of the gas it is detected by in-situ Hα monitors either at t = 1120 ms or t = 1123 ms (see vertical bars).

As it can be appreciated in the right column of figure 1, the shown global parameters of the three discharges evolve almost identically with time before the H_2 pulses injection. Then, past some milliseconds after their respective perturbations, these parameters seem to indicate that the behaviour of shots #24006 and #24009 comes again to be the same. Nevertheless, there are some monitors that indicate that the evolutions of these two shots have been markedly different during a short time interval.

To illustrate this difference, figure 2 shows the comparison of a more detailed view of the NBI phase (starting 10 ms after ECRH has been turned off) of shots #24001, #24006 and #24009. Now we show in the first row the evolution of the electron density together with the Hα signal from a monitor well apart from any of the injection points; in the second row, the magnetic fluctuations power spectra; in the third, the integrated (1-500 kHz) intensity of magnetic fluctuations together with the ratio n_e/Hα; and in the fourth, the time evolution (with a time resolution of 20 μs) of the reconstructed local emissivity in the region $0.7 \leq \rho \leq 1$. As in figure 1, the small vertical bars mark the times at which the pulses begin to effectively affect the plasma, i. e., the electron density starts increasing and the Hα signal drops. Although apparently the figures shown in the central and right columns are rather similar, a clear difference is observed, for instance, in the traces of Hα emissions: while in shot #24009 the highly fluctuating signal behaviour is transiently reduced, in shot #24006 it remains almost steadily at its lowest values for about 10 ms. The same applies to the power spectra, where all magnetic fluctuations, the broad band and the coherent m=5 rotation modes, are transiently reduced in shot #24009 and almost fully suppressed in shot #24006. It is remarkable that, except during the periods of relevant Alfvénic activity (like the one clearly detected in the spectrum of shot #24001 from 1130 to 1150 ms), the total intensity of magnetic turbulence mirrors the ratio n_e/Hα. Taking this ratio as a proxy of the particle confinement time, it could be said that, in fact [12], the clear (inverse) correlation between plasma outflows and rotation modes indicates that low frequency magnetic fluctuations are strongly linked to transport.

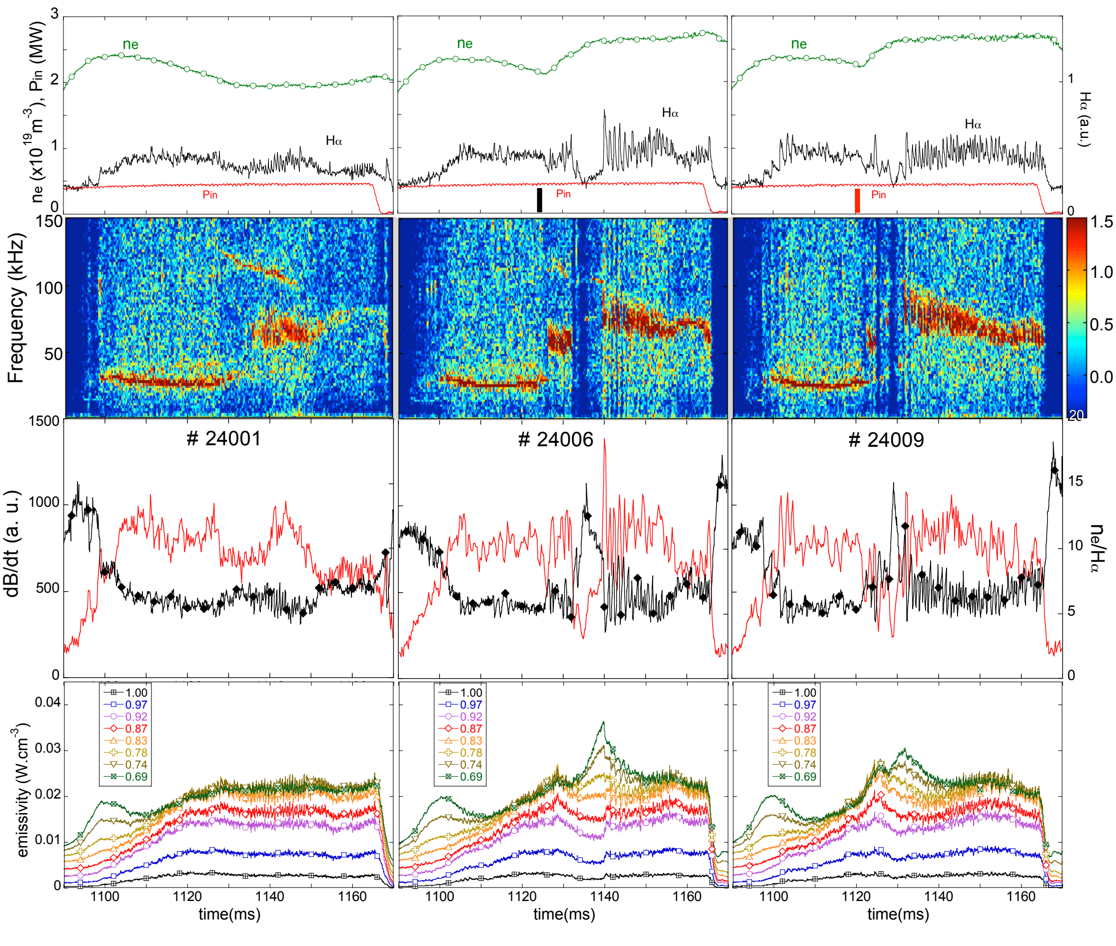

Figure 2. First row: Evolution of the electron density (continuous line with open circles), Hα signal detected far from the injection ports (dark continuous line) and input power from discharges #24001 (left column), #24006 (central column) and #24009 (right column); second row: Power spectrum of magnetic fluctuations detected with a Mirnov coil. Shot #24006 goes transiently through a clean H-mode phase, from 1132 to 1140 ms; third row: Integrated (1-500 kHz) magnetic fluctuations (light curves) and ratio ne/Hα (dark curves with symbols); fourth row: Time evolution of the local emissivity close to the plasma periphery, from $0.69 \leq \rho \leq 1$.

With respect to the behaviour of plasma emissivity in the plasma periphery, it can be seen that the evolution of radiation in shots #24006 and #24009 is also analogous to that of the reference discharge (#24001) during the building of plasma profiles in the NBI heating phase (see in figure 5, section 3.2, the detailed simulation of electron density and temperature profiles from the early ECRH phase, in 1040 ms, until 1134 ms) until their respective injection times. However, although the voltage in the gas valves was the same, the effect of the H_2 pulse is different in the two perturbed discharges: while in shot #24006 a bifurcation in the temporal evolution of emissivities from neighbour radial locations with respect to an "inversion radius" (namely $\rho \approx 0.83$) –typical signature of a local transport barrier [10]– is observed, in shot #24009 only a brief attempt of bifurcation takes place. Then, about 20 ms after the injections, peripheral radiation seems to converge to similar values in both discharges.

In the upper row of figure 3 we have plotted, from left to right: the profiles of electron density and temperature and the local emissivity, at the TS firing time instants, from the three studied discharges. There it can be seen the clear differences (bell-dome-bell) of electron density profiles shape and a less pronounced, but still apparent, change in the shape of electron temperature (but opposite trend: wide-narrow-wide) and emissivity profiles. Nevertheless, our interest is to compare the time evolution of the complete radial profiles of emissivity to look for possible differences between shots #24006 and 24009 as a consequence of the short establishment of the small edge barrier in shot #24006.

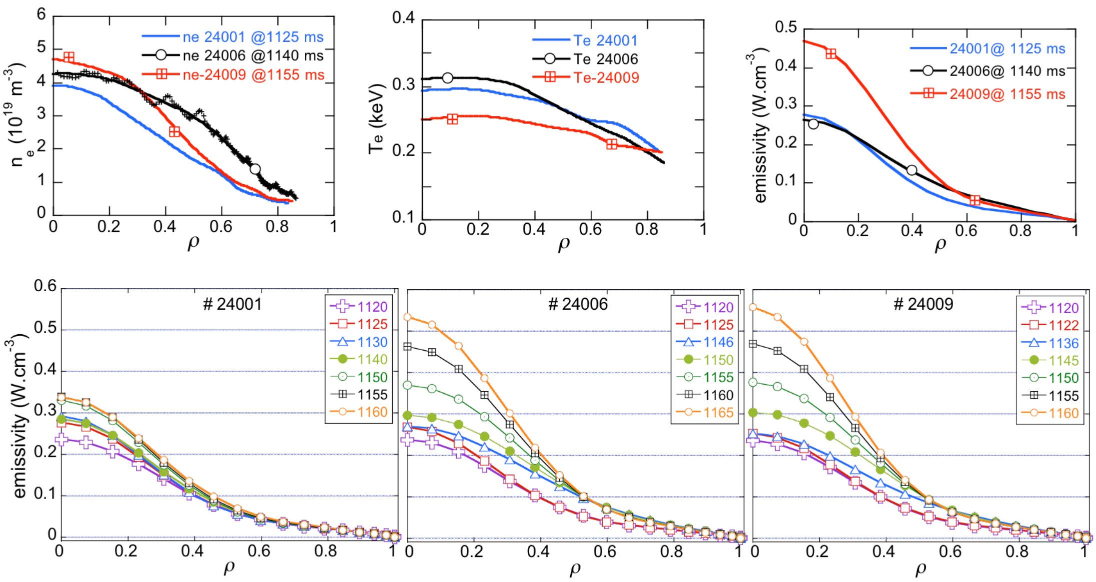

Figure 3. Upper row: experimental profiles of electron density, electron temperature and emissivity at the TS firing time instants for discharges #24001 (bell), #24006 (dome) and #24009 (bell). The raw data of electron density of shot #24006 are represented with small black crosses; lower row: emissivity profiles of the three shots at the indicated times in ms.

In the lower row of figure 3 we have drawn the radial profiles of emissivity at several selected time instants for each discharge. The plot in the left contains seven profiles, which show the evolution of radiation profiles in the reference discharge #24001. As it is visible, the radiation at the periphery stays almost constant in time (see the time evolution of peripheral emissivity in figure 2), from the starting profile, at 1120 ms, until the last represented profile at 1160 ms, while core radiation is slowly but continuously increasing. This is the typical behaviour of freshly Li-coated L-mode plasmas in TJ-II. Central and right boxes contain equivalent profiles of shots #24006 and #24009. Together with the unperturbed (common and identical) profiles at 1120 ms (thick purple line with crosses), we are showing the profiles which better evidence how deep is the perturbation that the pulse injection produces in each discharge and its duration. The red line with open squares represents the last unperturbed profiles, at 1125 ms and 1122 ms, respectively. The pulse injection provokes a slow and progressive profile change, that clearly departs from the time evolution seen in the reference discharge. The thick light blue curve with open triangles, at 1146 and 1136 ms, respectively, marks the maximum dome-like shape profiles attainable. After that time, again peripheral radiation stays almost constant and core radiation (approximately in $0 \leq \rho \leq 0.6$) continuously increases until the end of the discharges (see profiles at 1150, 1155, 1160 and 1165 ms in central panel and their equivalent at 1145, 1150, 1155 and 1160 ms in the right panel). It is worth noticing that discharge #24006, the one with the brief edge barrier, needs more time to recover the tendency of increasing central radiation than shot #24009 does, because the profile flattening period lasted 7 ms more (from 1125 to 1146 ms versus 1125 to 1136 ms).

3. Transport simulations

3.1. Transport model

The transport model consists of conservation equations for the electron density, n_e, and the electron and main ion (hydrogen) energy densities, respectively $n_e T_e$ and $n_i T_i$. The ion density is related to n_e by way of an effective charge, $Z_{\text{eff}}(\rho) = 1 + (Z_{\text{eff0}} - 1)(n_e(\rho)/n_{e0})^{1/4}$, where Z_{eff0} and n_{e0} are values at the magnetic axis characterized by $\rho = 0$ in the normalized radial coordinate (proportional to the square root of the enclosed plasma volume). This formula for Z_{eff} only intends to make a smooth relation between the effective charge and the plasma density. We have set $Z_{\text{eff0}} = 1.3$, a typical value for the kind of discharges used in this experiment. Then the ion density is defined as $n_i(\rho) = n_e(\rho)(Z_I - Z_{\text{eff}}(\rho) + 1)/Z_I$ where $Z_I = 6$ is the atomic number of the main impurity. In spite of this simplification in the ion density, we have considered the evolution equations for the densities of three charge states of carbon, n_{C2}, n_{C3} and n_{C4}. The sub-indexes refer to the charge state, so the respective species in spectroscopy notation are C_{III}, C_{IV} and C_{V}. Therefore, and using a sub-index j for plasma species, we have the following set of transport equations:

(1) $\partial_t n_e = -\nabla \cdot \boldsymbol{\Gamma}_e + S$

(2) $\partial_t \left(\frac{3}{2} n_{\{e,i\}} T_{\{e,i\}}\right) = -\nabla \cdot \mathbf{q}_{\{e,i\}} + P_{\{e,i\}}$

(3) $\partial_t n_{C2} = n_e[n_{C3} R_{C3} - n_{C2}(R_{C2} + I_{C2})] - \nabla \cdot \boldsymbol{\Gamma}_{C2}$

(4) $\partial_t n_{C3} = n_e[n_{C2} I_{C2} - n_{C3}(R_{C3} + I_{C3}) + n_{C4} R_{C4}] - \nabla \cdot \boldsymbol{\Gamma}_{C3}$

(5) $\partial_t n_{C4} = n_e[n_{C3} I_{C3} - n_{C4}(R_{C4} + I_{C4})] - \nabla \cdot \boldsymbol{\Gamma}_{C4}$

where the fluxes are:

(6) $\boldsymbol{\Gamma}_j = -\left(D_{\text{NC},j} + D_{\text{tb},j}\varepsilon\right)\nabla n_j = -D_e \nabla n_j$

(7) $\mathbf{q}_j = -n_j\left(\chi_{\text{NC},j} + \chi_{\text{tb},j}\varepsilon\right)\nabla T_j + \frac{5}{2}\Gamma_j T_j$

with transport coefficients to be defined later. Γ_j represents the flux-surface average component of the corresponding vector $\boldsymbol{\Gamma}_j$ perpendicular to the assumed flux surfaces. The sources and sinks in equations 1 and 2 are: the electrons from recycling and gas puffing, S_{rec} and S_{gp}, and from the neutral-beam injectors, S_{NBI}; the electron-ion Coulomb heat exchange P_{ei}, the NBI power density to the electrons or ions, $P_{\text{NBI},j}$; the power density from the electric work on the radial fluxes, $P_E = -e\Gamma_e E_r$; and the power density due to radiation and charge exchange, P_{rad} and P_{CX}:

(8) $S = S_{\text{rec}} + S_{\text{gp}} + S_{\text{NBI}}$

(9) $P_e = -P_{ei} + P_{\text{NBI},e} - P_{\text{rad}} + P_E$

(10) $P_i = P_{ei} + P_{\mathrm{NBI},i} - P_{\mathrm{CX}} - P_E$.

The terms S_{rec} and S_{gp} are calculated using an adaptation of the EIRENE code to the geometry of the TJ-II (see the documentation in [13]). The NBI sources use, as input, the 3-D distribution of neutrals after each EIRENE calculation for the given plasma profiles and confinement time. The Monte Carlo code FAFNER [14] is used to estimate S_{NBI} and $P_{\mathrm{NBI},j}$. All these sources are updated during the evolution with a period smaller than typical confinement times [15].

The model does not intend to describe radiation losses P_{rad} in Eq. (9), which are instead taken from experimental data as smooth profiles reconstructed every 1 ms. However, equations 3–5 provide a numerical diagnostic to give an approximate behaviour of the near-edge radiation that will be used to check the detailed perturbation to the emissivities when the transport barrier dynamics is simulated. The source and sink terms in equations 3–5 have been simplified to include only the 1-electron recombination and ionization rates, respectively R_{Cj} and I_{Cj}, taken from [16, 17] and dependent on the electron temperature. The choice of these species responds to two facts. First, carbon is a main impurity in TJ-II plasmas; second, at temperatures in the range of those typically found near the plasma edge of TJ-II NBI plasmas, there is a notable jump in recombination rates between species C_{IV} and $\mathrm{C_V}$. Therefore, we represent the impurities near the edge region via these carbon species using the set of equations 3–5, instead of a (not appropriate here) coronal equilibrium. The line-radiation losses of these carbon species are then described using cooling rates C_{Cj} from [18]:

(11) $P_{rad}^{C*} = n_e\,(C_{\mathrm{eff}} n_I + C_{C2} n_{C2} + C_{C3} n_{C3} + C_{C4} n_{C4})$.

The boundary conditions (ρ =1, indicated with sub-index a) are $n_{C4a} = 0$ in equation 5 and $n_{C3a} = 10^{-3}\, n_{ea}$ in equation 4. For equation 3 we fix an inwards flux at the last closed flux surface. In this way, the rate of incoming $\mathrm{C_{III}}$ redistributes the carbon species through the system of equations 3–5 according to the evolution of plasma profiles. All diffusivities here are taken equal to D_e (Eq. 6).

Transport fluxes in equations 1 and 2 have a neoclassical and a turbulent component, both expressed only as corresponding diffusivities (equations 6 and 7). For the neoclassical part, we have chosen formulations provided in [19, 20] to obtain $D_{\mathrm{NC},j}$ and $\chi_{\mathrm{NC},j}$ from the ambipolar radial electric field E_r as explained below. In both cases, the effective ripple can be used to obtain radial electric field profiles similar to the experimental ones. The resulting transport coefficients (only diagonal elements of the transport matrix are used here) are then adjusted through a fixed proportionality factor. Provided this, both descriptions of the neoclassical transport yield comparable results. The convenience of these semi-analytical methods is based on their ability to approach the electric potentials of TJ-II plasmas, both experimental and calculated with drift kinetic solvers, given experimental density and temperature profiles [21]. The anomalous contribution to transport is based on a resistive ballooning formulation [22] from which the linear growth γ_{RB} and saturation levels of turbulence can be obtained based on plasma parameters. This can be used on a fast equation for the evolution of such turbulence levels, ε:

(12) $\partial_t \varepsilon = (\gamma_{\mathrm{RB}} - \alpha_1 \varepsilon - \alpha_2 |\omega_s|)\varepsilon - \nabla \cdot \boldsymbol{\Gamma}_\varepsilon$.

The functions in equation (12) are a linear growth-rate and a saturation coefficient,

(13) $\gamma_{\mathrm{RB}} \propto \left(\frac{\eta\beta}{a\tau_A \epsilon} \frac{|p\prime|}{\rho\iota^2}\right)^{2/3}$

(14) $\alpha_1 \propto \frac{|p'|}{p}\, \gamma_{\mathrm{RB}}^{3/4} \sqrt{\frac{a\hat{s}}{\eta\sqrt{\tau_A}}}$,

where η is the resistivity, β is the typical ratio between diamagnetic and magnetic energy, τ_A is the Alfvén time and ϵ is the inverse aspect ratio (see all the details in [23,24]); and a shearing rate ω_s that is kept as a mechanism to provoke transport barriers [25]. In brief, by inspection of equation 12 with negligible diffusion and shearing ω_s, one can see that $\gamma_{\rm RB}$ provides an initially exponential growth and a saturation level $\sim \gamma_{\rm RB}/\alpha_1$. The presence of some ExB flow shearing will cause a decrement of ε, eventually making it drop to zero when the condition $\alpha_2|\omega_s| = \gamma_{RB}$ is approached—another stable solution in the absence of diffusion. With this transition model we find that the discharges in figure 1 are close to critical using $\alpha_2 = 1$. Since we do not need a verification of the turbulence model but just a mechanism for transport barrier dynamics, we take α_2 as a parameter to activate or not such dynamics. Indeed, equation 12 is the basis for different bifurcation models (of which [23–25] are examples) depending on the formulae for growth rate and saturation terms (13 and 14) and transport equations affected; but always the diffusive flux Γ_ε in equation 12 is comparatively small because the main dynamics must come from the competition between growth and suppression rates. Using a cylindrical coordinate r, we have $\omega_s = \partial_r E_r + (\hat{s} - 1)E_r/r$, where $\hat{s}$ is the magnetic shear. Note that we are considering ExB advection as the main agent capable of suppressing turbulence via flow shearing [26].

The transport coefficients that we use for the anomalous part are proportional to ε through coefficients $D_{tb,j}$ and $\chi_{tb,j}$ in equations 6 and 7. These, together with the neoclassical transport coefficients, close the system of transport equations. All the transport calculations have been done using the Astra package [27] conveniently expanded with peripheral codes to provide sources or other terms that require intensive calculations [28]. All the features of the transition model [19] are preserved after porting to Astra, as checked in [29] for a tokamak case, but the main difference now is that we use the transition model for a stellarator and the mechanism that modifies the radial electric field, and hence ω_s, is *only* the neoclassical electric field obtained by taking to steady state the equation

$$(15) \quad \partial_t E_r = \frac{e}{\epsilon_\perp}(\Gamma_e - \Gamma_i)$$

at frequent updates during the transport calculations. $\epsilon_\perp$ is the perpendicular dielectric constant. Since we consider the anomalous fluxes as intrinsically ambipolar, the right-hand-side in Eq. 15 contains only the neoclassical radial fluxes.

3.2. Reference case

We have performed several simulations based on data from the series of discharges described above, where good repeatability allowed for a better characterization of density and temperature profiles from Thomson Scattering data. Fixed multipliers in the transport coefficients are set to mimic the plasma behaviour of the reference case (#24001, no gas pulse), and then the same model is used with pulses (see next subsection).

In figure 4 we plot the simulated evolution of the volume averaged density and central electron temperature for parameters taken from TJ-II discharge #24001 (see experimental traces in Figure 1) together with the electron and energy confinement times as obtained with the two different formulations of the neoclassical transport, Kovrizhnykh's [19] in figure 4a and Beidler's [20] in figure 4b. Despite the simplified formulations, especially concerning the magnetic geometry of the device, these semi-analytical models are appropriate for transport modelling after adjusting the effective ripple [21]. The full symbols indicate volume averaged density (squares) and central electron temperature (circles) from TS at different times of similar discharges. Both in experiments and simulations, the ECRH power stops at t = 1080 ms causing a sudden drop of the electron temperature and a large increment in neutrals and, consequently, an increased particle source. Later on, from approximately t = 1090 ms to t = 1120 ms, the density and temperature profiles readjust until reaching a new steady state with higher confinement times according to the calculations, but in agreement with values presented elsewhere [3, 30]. These figures illustrate the margin of differences allowed in the calculations and, most importantly, the qualitatively similar response in terms of confinement times. This is important because, we must recall, once the transport model is chosen the evolution is done self-consistently from the early ECRH phase (t = 1050 ms in figure 4) considering the feedback between particle confinement times, wall recycling and NBI power and particle deposition. Despite the similar behaviour, we have adopted Beidler's description of the neoclassical transport coefficients to study the effect of gas pulses on the transport model. In this case, the effective ripple that enters the formulation is exponential in radius, as in [31], $\log\epsilon_{\mathrm{eff}} = -1.7 + 0.5\rho$.

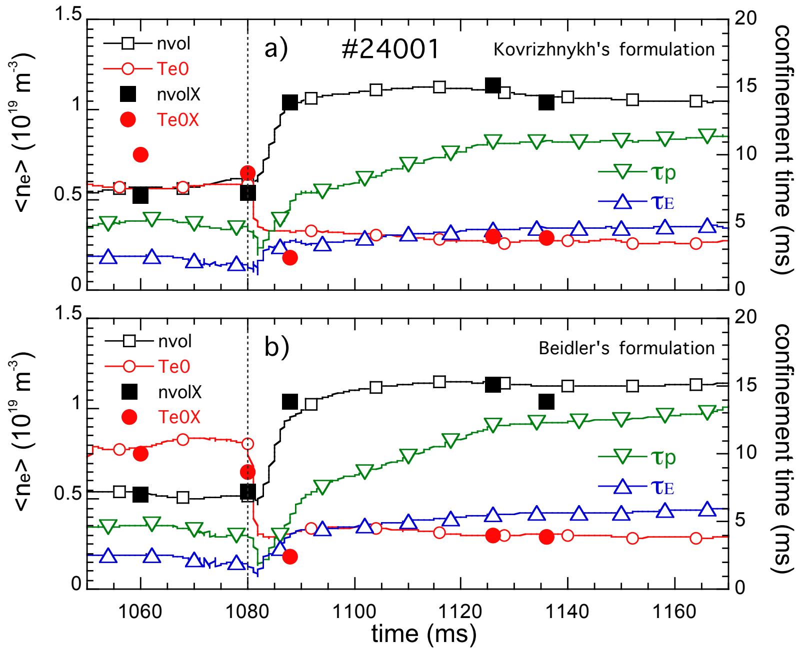

Figure 4. Calculated time traces (lines and open symbols) of the volume averaged density (squares), central electron temperature (circles), and particle and energy confinement times (triangles). Experimental density and temperature from repetition discharges are represented with respective full symbols. The two runs correspond to Kovrizhnykh (a) and Beidler (b) formulations of the neoclassical fluxes and corresponding ambipolar electric fields.

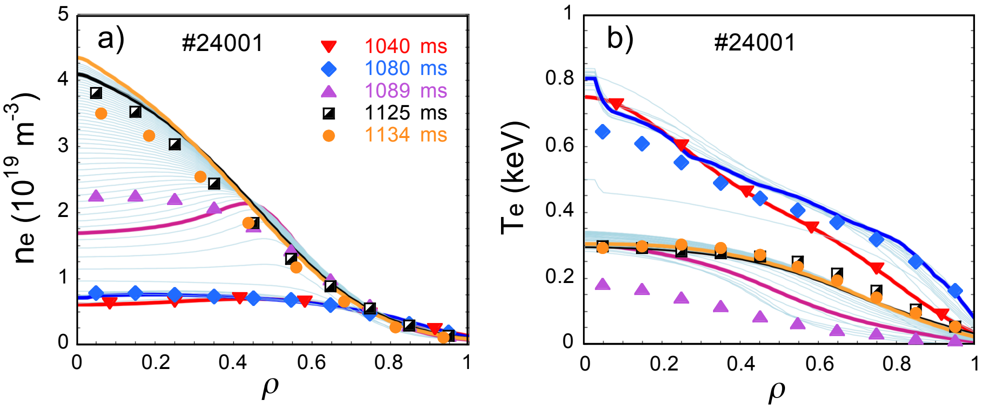

Figure 5. (a) Experimental profiles of electron density –symbols– taken from discharges similar to TJ-II #24001 (black squares represent profiles of shot #24001 shown in figure 3) at the times indicated, and simulated evolution with the transport model –thick lines– in corresponding colours. Light lines correspond to intermediate profiles during the evolution. (b) The same for electron temperature.

It is important that the transport model describes also the evolution of the density and temperature profiles, not just integral values. Figure 5a presents, with symbols, TS data from repetitions of discharges that give experimental information about how the profiles evolve from the ECRH to the NBI phase. The lines correspond to the transport calculation using gas puffing data and NBI parameters taken from the experiments. The times that coincide with the experimental data are highlighted with corresponding colours and indicated in the legend. Figure 5b is the same for the electron temperature profiles. For both profiles, figure 5 indicates that the transport model gives enough description of their evolution. Therefore we adopt it to study the effect of gas pulses.

3.3. Effect of a gas pulse in close-to-critical plasma

Before discussing the effect of a gas pulse when a bell-to-dome profile change is detected, it is in order studying how the model responds to moderate gas pulses if transport barrier dynamics are *not* allowed. Such cases are found experimentally [2] and we know that there is a threshold, related with the plasma density at the trigger of the gas pulse or the intensity of the pulse, that separates plasmas that show transport barrier dynamics from those which do not. Since the details of such threshold are unknown and we do not pretend completeness of the anomalous transport model given by Eq. 12, we study the response without transport barrier formation by just setting a small enough α_2 in Eq. 12. In Figure 6 we see the evolution of several profiles in response to the gas pulse (1123 ms < t_{pulse} < 1128 ms) corresponding to the simulation of discharge #24009. In agreement with the experiments, the edge electron density barely increases despite the increased source; but the electron temperature decreases noticeably.

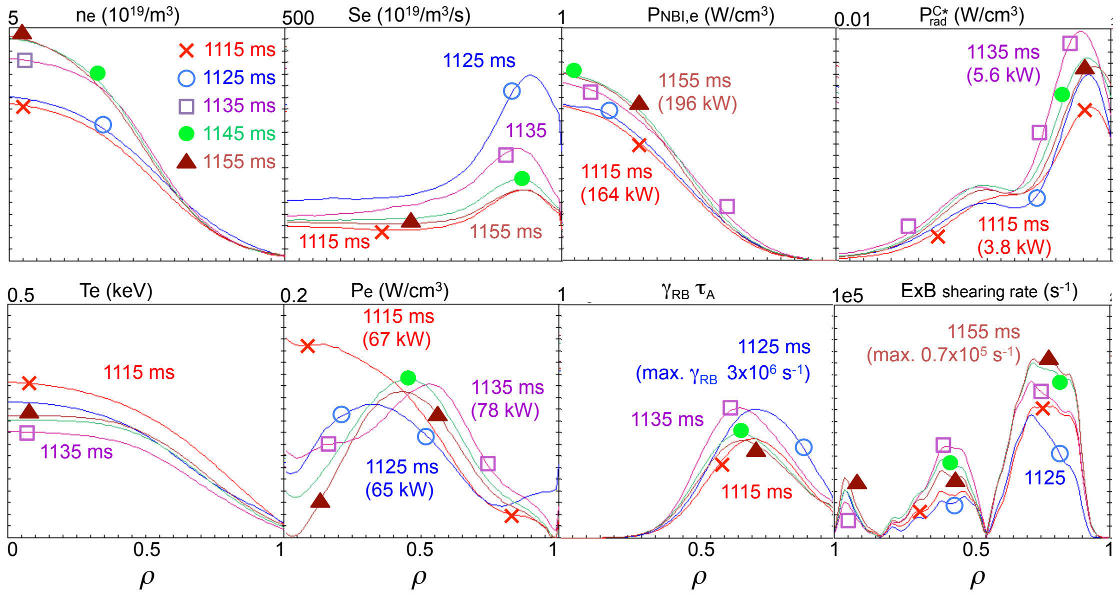

Figure 6. Simulated time evolution of profiles in response to a hydrogen pulse. From left to right and top to bottom: electron density, net electron source, NBI power density to electrons, power density of line radiation from carbon species, electron temperature, net electron heat source, RB turbulence growth rate (Ec. 13 normalized to the poloidal Alfvén time) and ExB shearing rate. Values in brackets of the power densities terms boxes are the volume integrated powers at the indicated times.

In the calculations, the decrement of the electron temperature is due to the balance of source and transport terms. In particular, the increased resistivity near the edge causes a larger growth of the RB transport (see Eq. 13); which, in addition to the smaller core temperature due to the larger core density, makes the electron temperature drop despite the also increased power density to the electrons. Other profiles that practically do not change during the sequence in figure 6 (not shown) are the ion temperature (average values around 70 eV) and the net NBI particle source. Additionally, we see that the shearing rate based on the neoclassical E_r increases due to the effect that the gas pulse has on plasma profiles. The specific values of γ_{RB} are important in their comparison with the ExB shearing rate. In the transition model based on equation 12, the transport barrier dynamics start at $\alpha_2\omega_s/\gamma_{RB} \sim 1/3$ [34], larger than in the present case. Finally, we also show the profiles of the radiated power density that corresponds to the evolving carbon charge states, P_{rad}^{C*}, and the integral values at two selected times (before the pulse and when the line radiation is highest for the profiles shown). In terms of global radiated power their emission accounts only for less than 20% (about 1.8 kW) of the total increment (close to 10 kW, see figure 1). However, in the peripheral region ($0.8 < r < 0.9$) the increment in emissivity due to the gas pulse, both for the calculation (P_{rad}^{C*}) and the experimental data (emissivity profiles in figure 3), is about 6 mW/cm3. This indicates that the three carbon species chosen for the radiation diagnostic are reasonably representative of the near-edge radiation.

Figure 6 illustrates a feature of the transport model: it is resilient to dome-type density profiles unless some mechanism provokes a local –in minor radius– and fast –much smaller time than a typical confinement time– decrement in the radial transport fluxes. Such local and fast reductions come from the shearing term in equation 12; but if it is unimportant or eliminated from the evolution (setting $\alpha_2 = 0$), the simulated plasma evolution after applying external gas pulses is always such that the density profiles grow keeping the bell-shape typically found during L-mode discharges, like in Figure 2. This has been checked in several variants of the transport model, e.g. using different descriptions of the neoclassical transport or changing the weights in the coefficients in equations 6 and 7, and is a consequence of the large transport in the edge region. Therefore, if nothing suppresses the anomalous component of the particle and heat fluxes in the model, the effect of a gas pulse behaves as in L-mode experiments [1, 2]: in the edge region (approximately $\rho > 0.75$) there is practically no change of the density of the electrons but their temperature decreases notably.

In order to compare with cases in which a transport barrier is transiently formed, we double the parameter α_2 in equation 12 (set to one for discharge #24009) to simulate discharge #24006. This activates the transition dynamics when the gas pulse is injected as will be shown below. In Figure 7, the upper plots represent calculated electron source terms for three discharges: TJ-II #24001 (reference discharge, no gas pulse), #24006 (gas pulse with transient dome profile) and #24009 (gas pulse and evolution with almost always bell-shaped density profiles). The figures show the profiles at the indicated times, i.e., the evolution due to the puffing in discharges #24006 and #24009. Corresponding density profiles are drawn in the middle boxes. The difference between the cases with gas pulse is that discharge #24006 is allowed to develop a transient transport barrier. Note that the effect of such transient barrier consists not only of making the density profile pass through a wider profile, but also the transiently larger confinement time decreases considerably the recycling source: the arrows in Figure 7 show how the source profile, after the jump due to the gas pulse ($t \approx 1130$ ms), drops more afterwards in the simulation of discharge #24006 than in #24009. Therefore, and always according to transport calculations, the decreased recycling sources are compensated by the improved confinement. The bottom panels in Figure 7 represent summed power density from the three carbon species used as diagnostic. Due to the local changes in density and electron temperature, the C^{3+} species develops a peak as shown for the simulated discharge #24006 at $t = 1145$ ms.

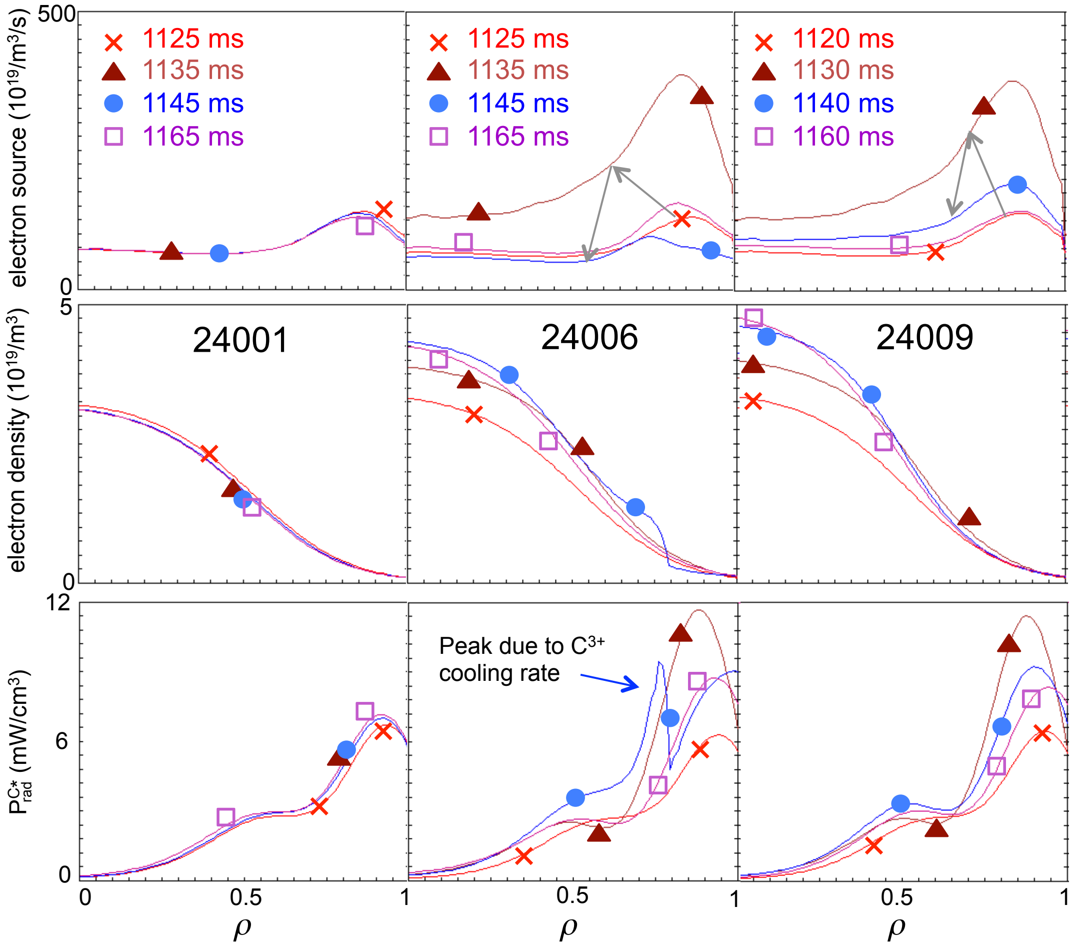

Figure 7. Simulated evolution of the electron source term S, Eq. 8 (top), corresponding electron density profiles (middle) and carbon radiation power densities (bottom), of three comparable discharges: reference (#24001), gas puffing with transient barrier and consequent dome profiles (#24006), and similar gas puffing —see figures 1 and 8— without transient barrier (#24009). The peak developed at t = 1145 ms for the radiation density is mainly due to the change of cooling rate of the C^{3+} species.

To better illustrate the differences between the two cases with gas pulse, in Figure 8 we compare the time traces of the simulation of discharges #24006 (transient barrier) and #24009 (no barrier). Interestingly, the similar response of the average density to a gas pulse in the simulated discharges is due to the different evolution of the particle confinement times. In the simulated discharge #24006, the decreased electron source is coupled to the increased particle confinement time, but the overall effect is a sustained raise of the density that resembles that of the simulated discharge #24009. Likewise, the energy confinement times are little sensitive to the gas pulse itself but not to the consequent evolution. Note that the deposited heating power is practically not sensitive to the formation of the barrier (see P_{NBI} line for discharge #24006 in Figure 8), but the net heat to the plasma species is quite altered. This is due to the combined effects of the edge radiation and electric field work in Eq. (9).

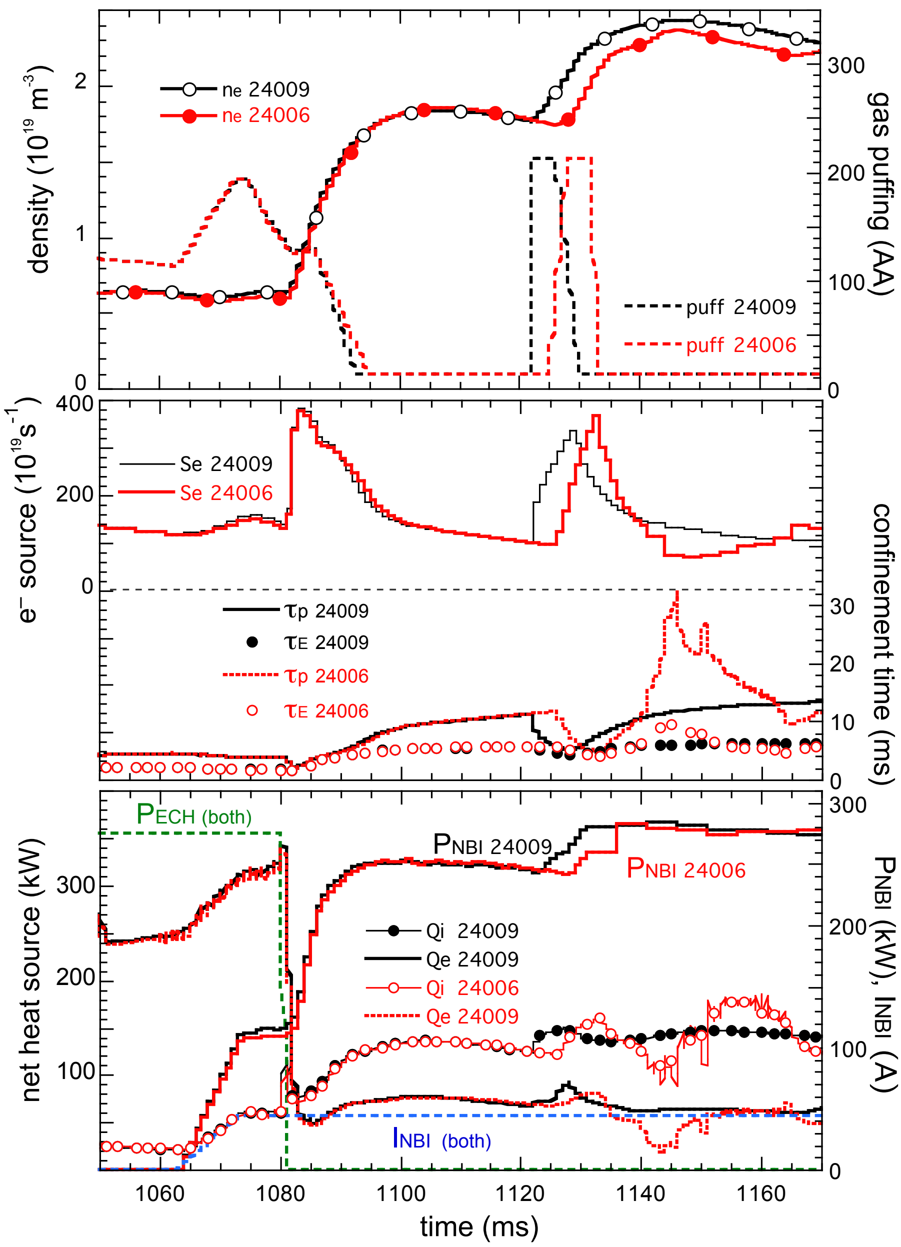

Figure 8. Time traces from the simulation of discharges #24006 and #24009. Line density and external gas puffing (up), net electron source and confinement times for electrons and plasma energy (middle); and power sources: net heat source terms for electrons or ions, absorbed ECR and NBI heating power and NBI current (bottom).

One of the interests of this transport analysis is to support the interpretation of the known evolution of the radiation emissivity profiles, which has been based on the transient establishment of a transport barrier near magnetic resonances [32]. The reason of having built a numerical diagnostic based on carbon emission is to see how the transport model describes (Eqs. 3–5), qualitatively but also quantitatively within order of magnitude, the near-edge radiation during these transient processes. Figure 9 is the time evolution of the radiated power densities coming from the indicated radial positions, from $\rho = 0.71$ to $\rho = 0.85$, according to the simulation. The transport barrier forms initially at $\rho = 0.76$, which is manifested in the existence of a pivot point that makes the behaviour at radii $\rho = 0.75$ and $\rho = 0.77$ diverge. The amplitude of the change in emissivities from neighbouring channels is on the order of 0.01 W/cm^3. Although a direct comparison with bolometry measurements cannot be done because the experimental data are affected by all atomic processes while the numerical diagnostic is based only on three carbon species, the basic features are reasonably well described as we can see in

Figure 2 (central box of the lower row): the emissivities, reconstructed from the real discharge #24006, reveal also perturbations on the order of 0.01 W/cm^3 when the barrier forms or is destroyed. Note that smaller perturbations can correspond to the repetitive breaking of a barrier that can also be appreciated in Figure 9.

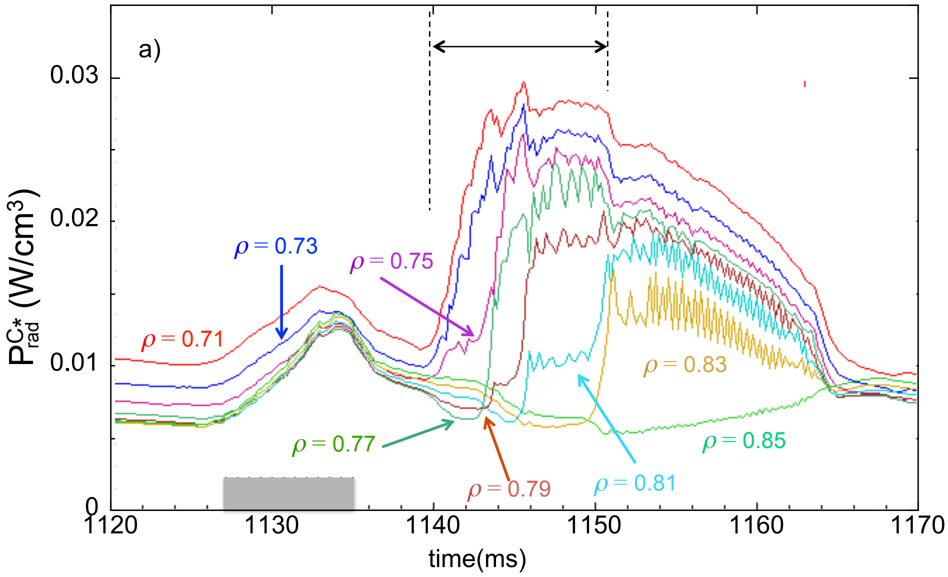

Figure 9. Simulated evolution of local emissivities (ρ = 0.71 to ρ = 0.85) in response to a gas pulse (shaded rectangle). A transport barrier develops at $t \approx$ 1140 ms (horizontal arrow indicates transport barrier duration) with a pivot point around $\rho = 0.76$.

3.4. Smooth confinement change: Effect of a gas pulse without barrier dynamics

As also mentioned in [1], TJ-II discharges heated by counter-NBI rarely show barrier dynamics like those of Figure 3 in co-NBI cases, the reason being that they generally start with rather dome profiles and remain so until the plasma quenches due to excessive edge cooling. In some cases, for example when there is additional heating with off-axis ECRH or when working at low densities in configurations free from low order rational values of the rotational transform near the edge, the edge remains hot enough and the plasma can be sustained during the whole NBI phase, ~100 ms. In these conditions there are no indications of barrier formation and the experiments with controlled H_2 gas pulses have shown a "soft" change in confinement after the gas pulse is applied. Figure 10 provides a comparison among discharges started with ECRH and continued with counter-NBI alone (port-through power 520 kW): discharges #21698 and #21702 have different densities due to slightly different densities in the target ECRH plasma. Due to the short gas pulse injection, discharge #21705 transits from the conditions of discharge #21702 to those of #21698. Observe that the pulse lasts only 5 ms but the plasma remains in the new, higher density state, to the end of the discharge (i.e., approximately 45 ms, significantly larger than the ~10 ms particle confinement time). We underline that no traces related to abrupt confinement changes are found, so the discharge can be said to undergo no transition and they will be simulated with small α_2 to avoid transport barrier formation. As in the previous cases, the sources may have changed as a consequence of the gas pulse because of changes in, e.g., NBI particle deposition. Otherwise, the gas pulse has promoted a change in confinement somehow associated to the change in plasma profiles. We investigate these aspects next.

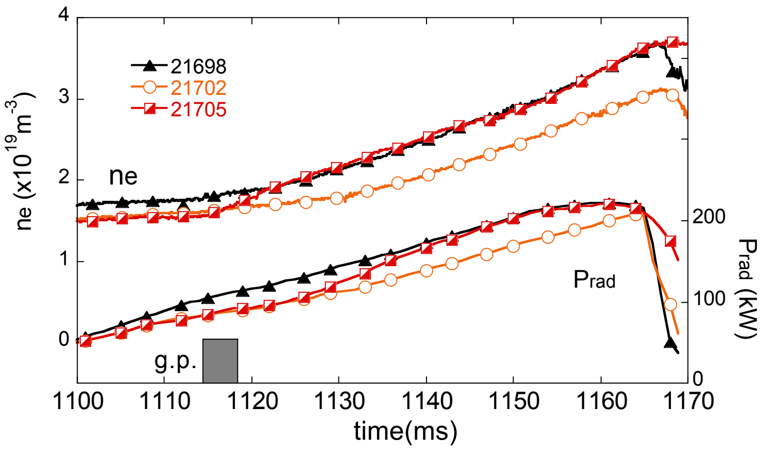

Figure 10. Comparison of TJ-II discharges with counter-NBI: discharge #21698 has slightly larger density at the beginning of the NBI phase, discharge #21702 has lower density, and discharge #21705 starts at low density but jumps to follow the higher density case aided by a short H_2 gas puffing (represented with a grey rectangle). The corresponding radiated powers are also plotted.

We simulate these discharges starting from initial conditions that give quasi steady-state evolution of the electron density. Then we apply a H_2 gas puffing pulse for one of the discharges with and without evolving electric field (see Figure 11). Since there is no transition dynamics in the experimental traces, we set a small $\alpha_2 = 1/3$ in equation 12 to recover conditions of negligible ExB shearing rate. In consequence, the only piece of transport that can respond to E_r is the neoclassical part.

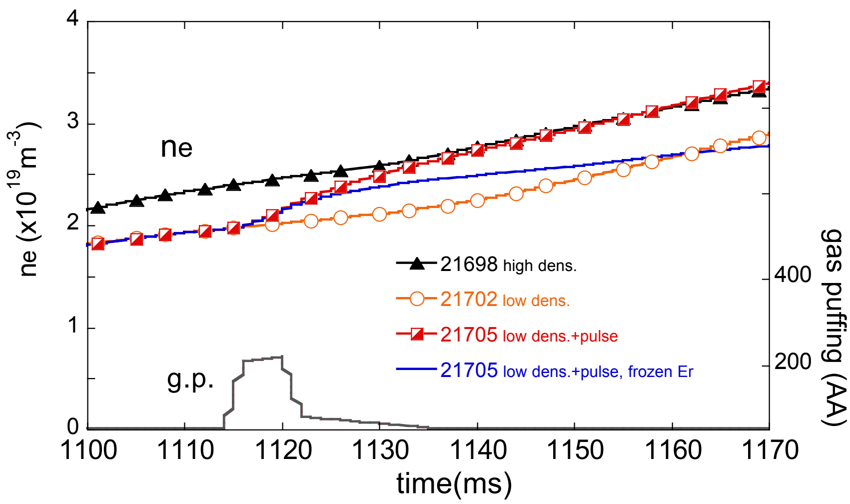

Figure 11. Simulated time traces of line averaged density for three discharges equivalent to the plotted in figure 10. The continuous (blue) line is the simulation of the discharge with gas puffing pulse for the case of keeping frozen the radial electric field from t = 1114 ms.

The case with gas puff pulse in Figure 11 (simulated discharge #21705, red continuous line + squares) reproduces a behaviour commonly found in L-mode NBI plasmas of the TJ-II: after the pulsed gas puffing, the profiles take the plasma to a state of better confinement, even if just slightly. Therefore, the modification of plasma profiles provoked by the gas pulse is an effective way of modifying the transport properties of the plasma. If the electric field is frozen just before the pulse (t = 1114 ms) for this same simulation, the plasma remains in the same confinement conditions and shows a quite different evolution (blue line). This proves that the effectiveness of the pulse in transport properties comes from the effect of E_r in neoclassical transport coefficients, which dominate in the plasma core according to the models used to reproduce TJ-II discharges in agreement with previous studies [33].

4. Discussion and conclusions

A transport model has been set so as to reproduce the time evolution of TJ-II discharges, i.e., ECRH phase, transition from ECRH to NBI heating phase, and establishment of bell-shaped plasmas during the NBI-only phase. If the target NBI plasma is in a threshold state for the formation of transport barriers, the injection of a cold gas pulse can provoke a transient passage through dome-type (H-mode-like) profiles. In terms of the transport model, the target plasmas are such that the suppression term $\alpha_2|\omega_s|$ is close enough to γ before the gas pulse, and the modification of plasma profiles due to the gas pulse augments the ExB-flow shear to critical values. The existence of a robust threshold state that shows limit cycle phenomena associated to barrier dynamics is a feature inherent to the transition model [34].

The importance of the transport model does not rely on its peculiarities (e.g. particular neoclassical formulation, turbulent transport model or turbulence suppression mechanism) but on its capability to reproduce the plasmas as an initial and boundary condition problem. The simulations can describe or explain the experiments because they incorporate the following fundamental elements:

i- High transport near the edge with non-linear dependence on the pressure profiles;
ii- the possibility of transport barrier formation and destruction, and
iii- E_r-dependent neoclassical transport coefficients.

The non-linear ∇p dependence of the radial fluxes is typical of anomalous transport models, the latter being a necessary addition to neoclassical fluxes in order to explain the results from balance studies in non-axisymmetric devices [35]. After trying different boundary conditions and sources (e.g. edge temperatures, NBI power within uncertainties, gas pulses of different strength), the density profiles are found resilient to change their initial bell shape. This is not surprising because such non-linear dependences of the fluxes on thermodynamic gradients tend to create profile stiffness (in our case, it is easy to see that the $\gamma_{\mathrm{RB}}/\alpha_1$ dependence of the dominant particle diffusivity near the plasma edge at negligible ω_s yields a dependence $D_e \propto L_p^{-5/6}$, where L_p is the pressure gradient scale length). More in general, any diffusivity that grows strongly enough towards the plasma edge will prevent the establishment of dome profiles (some illustration is given in the Appendix). Such growth is guaranteed in our case by the resistive ballooning model, which, in consequence, is responsible for the typical bell-shaped profiles of the simulated TJ-II L-mode plasmas.

The suppression term in Equation (12) changes drastically the L_p dependence of the transport coefficients, thus allowing for a rapid change of profile shape from bell to dome. From the transport simulation we learn that the experimental time-traces, notably the local emissivities, are quantitatively compatible with the true formation of a transport barrier (see figure 9), even if it happens in a transient or rapid manner. In agreement with [21], the ambipolar radial electric field is suited to eventually sustain a high shearing rate and therefore a H-mode plasma according to this turbulence-suppression mechanism, although the trigger might come from some other mechanism that promotes charge unbalance. In fact, this kind of signatures appears strongly related with the presence of low order rational values of the rotational transform close to the periphery [32, 36]. Note that discharges in figure 1 belong to a magnetic configuration with the rational value 8/5 around $\rho \approx 0.7$.

The modification of profiles through a gas puffing pulse can alter transiently the plasma profiles and, correspondingly, the electric field and the collisional transport. This mechanism should be always operative. Indeed, even though we have shown the experimental traces in Figure 10 to illustrate a case of smooth confinement change, already the comparison between discharges #24001, #24006 and #24009 in Figure 1 proves that the short gas pulse promotes a different confinement state: the densities do not return to the lower values of #24001 during the rest of the discharge. With our present estimates of particle and heat source evolution, this cannot be explained due to changes in the sources but due to the different confinement time. In this way, a good knowledge of collisional transport and its relation with E_r should provide well grounded ways to explain how to drive the plasmas to optimum confinement states via short gas pulses or, more in general, plasma shaping using appropriate sources. Concerning confinement control in stellarators, this work abounds on the importance of collisional transport and related electric field discussed in [37].

Now, we consider the suggestions of previous studies [1, 2], namely, that the behaviour of the profiles regarding bell and dome shapes is related with the modifications of NBI heating efficiency in the core due to CX losses near the edge. As the authors in [1] note, spontaneous transitions between profile shape (bell-dome) share the same signatures as those forced with gas pulses, which agrees with the confinement change proposed with the model via transport barrier development. Still, the importance of CX losses of the high-energy ions from the beam should be estimated and compared with bolometry measurements. These (see Figure 12) show a clear lowering of the core radiation simultaneous with an increment of the edge radiation. The model agrees with this because there is indeed an increment in edge radiation from our diagnostic carbon states and a decrement in core electron temperature at roughly constant density, i.e., the net radiation should decrease. However, the estimate of heat sources from NBI is based on the flux surface averaged distribution of neutrals previously calculated with EIRENE, while, in reality, the neutrals distributions are not flux surface functions and present strong asymmetries with respect to the magnetic configuration. Neither these asymmetries nor the plasma composition have been considered in this study. As a final exercise, we have evaluated the impact of having a different density of neutrals in the evaluation of NBI heat sources in the core. Multiplying by ten the atom density with respect to the (average) neutral atom profiles used in the calculations at the time of gas puffing, we obtain that the net power to the electrons reduces to a 68%, while the core power density lowers from roughly 0.7 MW/m^3 to 0.6 MW/m^3. This is a significant change that might explain figure 12, but it has not been modelled because the uncertainties in the 3D neutrals distribution are large. Likewise, we have checked that the effective charge can have a similar impact in power deposition, but we have not considered it in the calculations of the NBI sources.

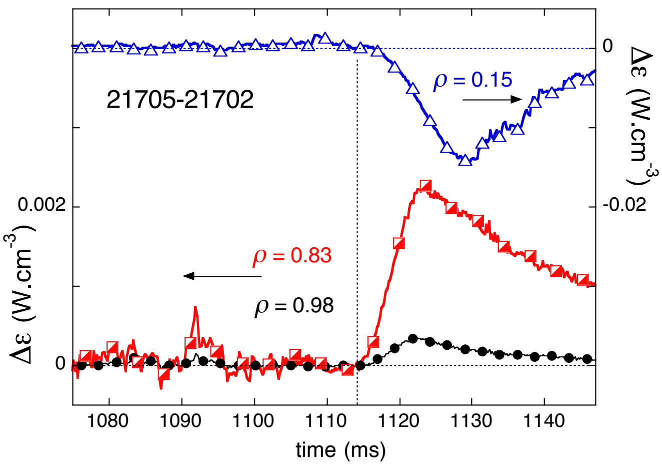

Figure 12. Departure of the local emissivity from the reference case (discharge #21702) when a gas pulse is applied (#21705). Data at different radii indicate increased emissivity near the edge (left ordinate) but decreased in the core region (right ordinate).

Aside from the effective charge and local neutral densities, future works should improve two important ingredients in the transport model to account for the modifications of E_r during the plasma evolution: the plasma edge (i.e.: the boundary values are imposed) and the radiation (only a few species are included to act as diagnostic). Edge cooling may induce changes in the radial electric field due to (i) intense enough cold gas entrance and recycling, (ii) reduced thermal outflow from the hot core in presence of, e.g., transport barriers; and (iii) enhanced impurity radiation caused by a reduction in their ionization state. Regarding point (iii), our results indicate that atomic physics near the barrier zone might become a significant contribution: as seen in Figure 7, locally abrupt changes in the radiation density of a charged impurity can take place in the density and temperatures of our plasmas for a common impurity (carbon in this case).

In summary, a transport model has been developed to study the evolution of TJ-II plasma profiles in response to short gas-pulses. It includes the possibility of forming transport barriers under strong enough sheared electric drift. The passage from bell to dome profiles in the density and radiation profiles after a gas pulse, associated to the L to H transition in TJ-II plasmas, is explained through the rapid formation of a transport barrier due to the shear of the neoclassical electric field. Even in the absence of transport barriers, confinement properties after gas pulses are found to change also due to modifications of the radial electric field.

Appendix

Here we consider the Gaussian profile as representative of bell-type profile in the cylindrical coordinate *r*. Let $n(r) = n_0\exp[-r^2/a^2]$ be the transported magnitude with constant n_0. By simple substitution we can see that, given a source $S(r)$, the Gaussian profile can be a solution to the steady state equation

$$S(r) = -\frac{1}{r}\partial_r(rD\partial_r n)$$

if the diffusivity is expressed as

$$D(r, \nabla p) = C(r)L_n^{-\alpha},$$

where $L_n = |\partial_r \ln n|$ and α is a real number. As expected from edge particle sources (recycling or gas puffing) we assume an electron-source profile with integral values that grow towards the edge,

$$S_I(r) = \int_0^r r'S(r')\mathrm{d}r'$$

and therefore the function $C(r)$ is

$$C(r) = \frac{a^{2(1+\alpha)}S_I(r)}{2^{1+\alpha}r^{2+\alpha}n(r)}$$

Acknowledgments

The authors are fully indebted to the TJ-II Team. This work has been supported by the Spanish Government via the “Programa Estatal de Fomento de la Investigación Científica y Técnica de Excelencia” (ENE2014-52174-P).

References

[1] Tabarés F.L. *et al* 2010 *Contrib. Plasma Phys.* **50** 610
[2] Ochando M.A. *et al* 2010 *37th EPS Conference on Plasma Physics* P1.1075
[3] Tabarés F.L. *et al* 2008 *Plasma Phys. Control. Fusion* **50** 124051
[4] Alejaldre C. *et al* 1990 *Fusion Technol.* **17** 131
[5] Ochando M.A., Castejón F. and Navarro A.P. 1997 *Nucl. Fusion* **37** 225

[6] Barth C.J. *et al* 1999 *Rev. Sci. Instrum.* **70** 763
[7] Baião D. *et al* 2012 *Rev. Sci. Instrum.* **83** 053501
[8] Navarro A.P., Ochando M.A. and Weller A. 1991 *IEEE Trans. Plasma Sci.* **19** 569
[9] Ochando M.A. *et al* 2006 *Fusion Sci. Technol.* **50** 313
[10] Sun B.J., López-Bruna D., Ochando M.A. and Pedrosa M.A. 2014 *41st European Physical Society Conf. on Plasma Physics, ECA (Berlin, Germany, 23–27 June 2014)* **vol 38** P2.090 (http://ocs.ciemat.es/EPS2014PAP/pdf/P2.090.pdf)
[11] Sun B.J., López-Bruna D., Ochando M.A. and Pedrosa M.A. 2015 *42nd European Physical Society Conf. on Plasma Physics, ECA (Lisboa, Portugal, 22–26 June 2015)* **vol 39** P4.162 (http://ocs.ciemat.es/EPS2015PAP/pdf/P4.162.pdf)
[12] van Milligen B.Ph. *et al* 2016 *Phys. Plasmas* **23**, 072305
[13] Reiter D. 2005 "The EIRENE code user manual (including: B2-EIRENE interface)," http://www.eirene.de/html/manual.html
[14] Lister G. 1985 "FAFNER: A fully 3-D neutral beam injection code using Monte Carlo methods," Tech. Report IPP 4/222, Max Plank Institute für Plasmaphysik, Garching, Germany, 1985
[15] de Bustos A. *et al* 2011 *Nuclear Fusion* **51** 083040
[16] Nahar S.N. and Pradhan A.K. 1997 "Electron-ion recombination rate coefficients, photoionization cross sections, and ionization fractions for astrophysically abundant elements. I. Carbon and nitrogen," The Astrophysical Journal Supplement Series, **111**, no. 1, p. 339, 1997
[17] Kobayashi T., Yoshikawa M., Kato T., Kubota Y., Saito M., Matama K., Itakura A., and Cho T., "Study of carbon ion behavior by using collisional radiative model in the GAMMA 10 tandem mirror," in New Research on Atomic and Molecular Processes and the Increasing Applications to Plasmas, Science and Technology, vol. 7 of Journal of Plasma and Fusion Research, (Nagoya, Aichi, Japan), pp. 45–49, The Japan Society of Plasma Science and Nuclear Fusion Research, October 2004
[18] Tokar M.Z. 1994 *Plasma Phys. Control. Fusion* **36** 1819
[19] Kovrizhnykh L.M. 2006 *Plasma Phys. Rep.* **32** 988
[20] Beidler C.D. 1996 "Neoclassical transport properties of HSR," Report 2/331, IPP-Garching
[21] Gutiérrez-Tapia C. *et al* 2015 *Plasma Phys. Control. Fusion* **57** 115004
[22] Carreras B.A., García L. and Diamond P.H. 1987 *Phys. Fluids* **30** 1388
[23] Delgado J.M., Garcia L. and Carreras B.A. 2009 *Plasma Phys. Control. Fusion* **51** 015003
[24] Garcia L., Carreras B.A., Lynch V.E., 1999 *Phys. Plasmas* **6** 107
[25] Carreras B.A., Newman D.E., Diamond P.H. and Liang Y-M 1994 *Phys. Plasmas* **1** 4014
[26] Kim Y.B., Diamond P.H., Biglari H. and Callen J.D. 1991 *Phys. Fluids B* **3** 384
[27] Pereverzev G.V. and Yushmanov P.N., "ASTRA Automated System for TRansport Analysis," Tech. Rep. IPP 5/98, Max Plank Institut für Plasmaphysik, Garching, February 2002
[28] López-Bruna D. *et al* 2010 "Programas periféricos de ASTRA para el TJ-II," Informes Técnicos Ciemat 1201, Ciemat
[29] López-Bruna D., Carreras B.A. and Newman D.E. 2000 *Nucl. Fusion* **40** 1825
[30] Estrada T. *et al* 2009 *Plasma Phys. Control. Fusion* **51** 124015
[31] Turkin Y., Beidler C.D., Maaßberg H., Murakami S., Tribaldos V. and Wakasa A. 2011 *Phys. Plasmas* **18** 022505
[32] López-Bruna D., Ochando M.A., López-Fraguas A., Medina F. and Ascasíbar E. 2013 *Nucl. Fusion* **53** 073051
[33] López-Bruna D. *et al* 2013 *Plasma Phys. Control. Fusion* **55** 015001
[34] López-Bruna D., Newman D.E., Carreras B.A., and Diamond P.H. 1999 *Phys. Plasmas* **6** 854
[35] Dinklage A. *et al* 2013 *Plasma Phys. Control. Fusion* **53** 063022
[36] López-Bruna D. *et al* 2011 *Plasma Phys. Control. Fusion* **53** 124022
[37] Maassberg H., Beidler C.D. and Simmet E.E. 1999 *Plasma Phys. Control. Fusion* **41** 1135